

## Article

# Enhanced Cycle Performance of NiCo<sub>2</sub>O<sub>4</sub>/CNTs Composites in Lithium-Air Batteries

Dae-Seon Hong<sup>1,2</sup>, Yeon-Ji Choi<sup>1,3</sup>, Chang-Su Jin<sup>1</sup>, Kyoung-Hee Shin<sup>1</sup>, Woo-Jin Song<sup>2</sup> and Sun-Hwa Yeon<sup>1,\*</sup>

<sup>1</sup> Department of Energy Storage Research, Korea Institute of Energy Research, Daejeon 34101, Republic of Korea; ghdeotjs345@kier.re.kr (D.-S.H.); choiyunji030@kier.re.kr (Y.-J.C.); csjin@kier.re.kr (C.-S.J.); khshin@kier.re.kr (K.-H.S.)

<sup>2</sup> Department of Organic Materials Engineering, Chungnam National University, Daejeon 35015, Republic of Korea; wjsong@cnu.ac.kr

<sup>3</sup> Department of Energy Engineering, HanYang University, Seoul 04763, Republic of Korea

\* Correspondence: ys93@kier.re.kr

**Abstract:** The lithium-air battery is a new type of secondary battery technology that is currently receiving a lot of attention in the field of power storage technology. These batteries are known to offer high energy densities and potentially longer driving ranges. In this study, NiCo<sub>2</sub>O<sub>4</sub> and CNTs were used to create a composite for use as the cathode of a Li-air battery. Improving the 3D needle-like structure that provides extensive transport channels for electrolyte infiltration and numerous sites facilitated charge transfer reactions and the synergistic effect of highly electrocatalytic NiCo<sub>2</sub>O<sub>4</sub> with pronounced activity and high conductive CNTs, with the synthesized NiCo<sub>2</sub>O<sub>4</sub>@CNTs composites exhibiting active catalytic performance for both OER and ORR reactions. It also showed improved cycle performance at high current densities. NiCo<sub>2</sub>O<sub>4</sub>@CNTs composites were successfully fabricated using a hydrothermal method together with a sequential annealing treatment. The components of the completed composite were confirmed using TGA, XRD, and SEM, and the specific surface area was analyzed using BET. The composite was performed for over 120 cycles at a current density of 200 mA·g<sup>-1</sup>, and 500 mA·g<sup>-1</sup> was achieved under the capacity limiting condition of 500 mAh·g<sup>-1</sup>. The charging/discharging characteristics were compared under various current densities, exhibiting stable cyclability. The high catalytic activity of NiCo<sub>2</sub>O<sub>4</sub> oxide supports its potential use as a cathode in Li-air batteries.



**Citation:** Hong, D.-S.; Choi, Y.-J.; Jin, C.-S.; Shin, K.-H.; Song, W.-J.; Yeon, S.-H. Enhanced Cycle Performance of NiCo<sub>2</sub>O<sub>4</sub>/CNTs Composites in Lithium-Air Batteries. *Energies* **2024**, *17*, 58. <https://doi.org/10.3390/en17010058>

Academic Editor: King Jet Tseng

Received: 15 November 2023

Revised: 7 December 2023

Accepted: 19 December 2023

Published: 21 December 2023



**Copyright:** © 2023 by the authors. Licensee MDPI, Basel, Switzerland. This article is an open access article distributed under the terms and conditions of the Creative Commons Attribution (CC BY) license (<https://creativecommons.org/licenses/by/4.0/>).

**Keywords:** lithium-air battery; air cathodes; lithium; carbon nanotube; NiCo<sub>2</sub>O<sub>4</sub>

## 1. Introduction

Fossil fuels still account for over 80% of the worldwide energy requirements and have a significant daily impact on global warming and environmental pollution [1,2]. Therefore, the further development of renewable energy options is considered an important step in the effort to address the issue of fossil fuel consumption. In particular, lithium-ion batteries (LIBs), first commercialized by Sony in the 1990s, have been widely used in various applications such as smartphones, laptops, and electric vehicles (EVs) in our daily lives [3]. In lithium-ion batteries (LIBs), through the process of ‘intercalation chemistry’, lithium ions move from an anode to a cathode during the discharge process, passing through the electrolyte and releasing electricity. However, current lithium-ion battery technologies still face various challenges such as high costs associated with limited lithium resources, safety concerns, and unsatisfactory energy densities [4]. Notably, the limited energy storage capacity of lithium-ion batteries (LIBs) serves as a limiting factor in extending the driving range of current electric vehicles (EVs) [5]. Therefore, the next step to enhance the electrical performance of the battery lies in the development of next-generation battery technologies such as lithium-sulfur as well as metal-air batteries, including Li-air and Na-O<sub>2</sub> batteries [6]. Lithium-air batteries are considered one of the most promising candidates to replace LIBs

due to their low weight, safety, and remarkably high theoretical energy density (approximately 3500 to 5200 Wh·kg<sup>-1</sup>), which is comparable to gasoline [7–11]. If its complete theoretical specific energy were to be fully extracted, the lithium-air battery would be the best substitute for fossil fuels in electric vehicles with plug-in capabilities, as it has the potential to offer up to 10 times the energy density of any other battery. In reality, the system yields a much lower specific energy than the theoretical value due to various shortcomings such as high overvoltage, slow kinetics of the oxygen evolution reaction (OER) and oxygen reduction reaction (ORR), the formation of insoluble discharge products in aprotic electrolytes, and difficulties in charge transfer between the solid discharge product and solid cathode. Therefore, researchers from various backgrounds have explored different aspects of the lithium-air system, all with the unified goal of commercializing rechargeable aprotic lithium-air batteries. The lithium-air battery idea was first introduced in 1976 using an aqueous electrolyte, but it failed due to the corrosion of lithium. In 1990, Abraham and Jiang achieved success in assembling a rechargeable lithium-air battery with excellent Coulombic efficiency and minimal overvoltage by using a non-aqueous electrolyte and an air electrode catalyzed by cobalt phthalocyanine [12]. Subsequently, investigations into the advancement of rechargeable aprotic lithium-air batteries have been heightened, focusing on improving their efficiency and cyclic stability [13,14]. To fully achieve the theoretical capacity of the lithium-air system, various configurations of Li-air batteries are under investigation [15]. Lithium-air batteries can be classified into four different types based on the electrolyte they use: aprotic (non-aqueous), aqueous, solid-state, and hybrid systems [16]. Among them, the aprotic (non-aqueous) systems have attracted more attention for their potentially higher energy density and cycle efficiency [17–19]. However, lithium-air batteries face challenges, particularly those related to electrolyte instability in oxygen-deficient conditions, reduced efficiency in the reversible cycling of Li metal anodes, and the degradation of catalytic materials [20,21]. The most critical issue is that the discharge products, Li<sub>2</sub>O<sub>2</sub> and Li<sub>2</sub>CO<sub>3</sub>, accumulate at the cathode, leading to declining cycling performance by interfering with the oxygen reduction reaction (ORR) and the oxygen evolution reaction (OER) [22,23]. An effective approach to address the aforementioned issue is to develop efficient and corrosion-resistant bifunctional electrocatalysts toward ORR and OER [24].

To address these issues, research has focused on investigating various catalysts. In aprotic lithium-air batteries, well-known catalysts like noble metal catalysts, cheap metal catalysts, and carbon-based catalysts are primarily being examined for their bifunctional catalytic efficacy. Metal oxides have been widely researched as bifunctional electrocatalysts due to their notable catalytic efficacy, minimal toxicity, accessibility, and cost-effectiveness. And transition metal oxide spinel structures have demonstrated effectiveness as bifunctional catalysts, which is attributed to their elevated electrochemical activity and electronic conductivity [25]. In addition, numerous studies have demonstrated that nanostructured architectures, along with the varied configurations of structural units, can serve as a way to adjust the properties of materials. In these designs, the needle-like structure of NiCo<sub>2</sub>O<sub>4</sub>-based composites can significantly enhance electrochemical performance through diffusion reduction paths for electrolytes and electrons [26]. It provides effective pathways for oxygen transfer and offers a substantial specific surface area along with abundant active sites [27]. The spinel-type NiCo<sub>2</sub>O<sub>4</sub> has attracted significant focus within the field of electrochemistry due to its excellent activity, high stability, environmental friendliness, and abundant resources [28–30]. One approach, particularly effective for enhancing electrochemical properties, involves creating oxygen vacancies on the surface through synthesis to activate the OER [31]. The oxygen defects in these materials are important [32]. The oxygen vacancies can significantly enhance the intrinsic conductivity, thereby improving electrochemical performance [33].

LABs are primarily composed of a porous cathode layer, a separator, a lithium anode, and an electrolyte. Frequently, porous cathode materials are combined with support materials of high conductivity. It is important to note that ‘support material’ refers only to a porous scaffold designed to accommodate Li<sub>2</sub>O<sub>2</sub> (ORR), rather than decomposing

$\text{Li}_2\text{O}_2$  (OER). Battery performance aspects such as energy efficiency, cycle retention, and capacity of LABs are significantly influenced by the support materials, and the properties of these support materials are crucial [34]. Specifically, the non-soluble discharge byproduct (mainly  $\text{Li}_2\text{O}_2$ ) is produced on the surface of the support materials. Consequently, the design of the support materials' structure should be thoughtfully considered to accommodate the discharge product and facilitate the diffusion of  $\text{O}_2$  gases and the penetration of electrolytes [35]. Carbon nanotubes (CNTs) are commonly employed in electrodes due to their outstanding conductivity, chemical stability, and large surface area [36,37]. However, the capacitance of CNTs is constrained by the mechanism for storing charge at the interface between the electrode and electrolyte [38]. Additionally, it is particularly difficult to disperse CNTs when creating the electrode slurry.

In this study, CNTs were treated with nitric acid to enhance their hydrophilicity, and the metal oxide  $\text{NiCo}_2\text{O}_4$  was synthesized through a hydrothermal and an annealing process. The process for preparing  $\text{NiCo}_2\text{O}_4$ @CNTs follows the same manufacturing steps as  $\text{NiCo}_2\text{O}_4$ , with the additional inclusion of nitric acid-treated CNTs at the initial stage.

The purpose of this study is to develop a cathode composite with a catalyst for the long-term operation of lithium-air batteries in air conditions. We created a composite using a  $\text{NiCo}_2\text{O}_4$  catalyst on CNTs using hydrothermal synthesis and annealing. The composite  $\text{NiCo}_2\text{O}_4$ @CNTs exhibited a significantly extended cycle life with lower overpotential compared to pristine CNTs.

We converted the conventional CNTs, which were originally used, into hydrophilic CNTs through a hydrothermal synthesis, making dispersion considerably easier. As a result, the synthesized final composite exhibited a longer cycle life compared to previously reported CNTs. Furthermore, the composite was found to have lower resistance than conventional CNTs using electrochemical impedance spectroscopy (EIS) measurements. The outstanding characteristics of the composite are attributed to its excellent OER/ORR reactions at the cathode. This can be considered a significant step toward achieving commercial lithium-air batteries.

## 2. Materials and Methods

### 2.1. Fabrication of Air Cathodes

Synthesis of the MWCNTs-COOH: 1 g of MWCNTs powder was stirred with 100 mL of  $\text{HNO}_3$  (Nitric Acid 70 wt %) at 90 °C for 2 h. After the reaction was completed, the resulting mixture was filtered, washed several times with D-I water and ethanol, and then vacuum dried at 100 °C for 12 h to obtain the final powder.

Synthesis of the  $\text{NiCo}_2\text{O}_4$ :  $\text{Co}(\text{NO}_3)_2 \cdot 6\text{H}_2\text{O}$  (1.098 g) and  $\text{Ni}(\text{NO}_3)_2 \cdot 6\text{H}_2\text{O}$  (0.549 g) were dissolved in water in a 2:1 molar ratio, and then 1.68 g of urea was added. The solution was stirred for one hour until a bright pink color appeared. Afterward, it was placed in a Teflon-lined stainless steel autoclave and then heated at 120 °C for 12 h. The paste obtained through the hydrothermal process was filtered and washed several times with water and ethanol. Subsequently, it was vacuum dried overnight at 100 °C. Finally, the precursor underwent 2 h annealing at 350 °C at a slow heating rate (2 °C·min<sup>-1</sup>) for the formation of  $\text{NiCo}_2\text{O}_4$ .

Synthesis of the  $\text{NiCo}_2\text{O}_4$ @CNTs:  $\text{Co}(\text{NO}_3)_2 \cdot 6\text{H}_2\text{O}$  (1.098 g) and  $\text{Ni}(\text{NO}_3)_2 \cdot 6\text{H}_2\text{O}$  (0.549 g) were dissolved in water at a molar ratio of 2:1, and then 1.68 g of urea, along with 0.3 g of MWCNTs-COOH, was added. Subsequently, the procedure was conducted exactly the same way as the  $\text{NiCo}_2\text{O}_4$  synthesis method.

### 2.2. Material Characterization

The structural phases of the samples were analyzed using X-ray diffraction (SmartLab High Temp, Rigaku, Tokyo, Japan) with the following parameters: Cu target ( $\lambda = 1.54056 \text{ \AA}$ ), working voltage 45 kV, working current 200 mA, and the  $2\theta$  scanning ranging from 10° to 80°. The micromorphology of the product was observed using field emission scanning electron microscopy (Regulus 8220, HITACHI, Tokyo, Japan). The specific surface area

of different samples was determined using a specific surface area and porosity analysis system (Belsorp max, Osaka, Japan).

### 2.3. Electrode Fabrication and Battery Measurement

The air cathodes were prepared by mixing three types of self-made powders and PVDF binders in a 9:1 ratio. Organic solvent NMP was used to create the slurry. Then, the prepared slurry was coated onto the prepared Gas Diffusion Layer (GDL) and vacuum dried at 100 °C for 12 h. The mass loading was calculated as the combined mass of oxide and carbon and was set at 0.5 mg/cm<sup>2</sup> ( $\pm 0.1$ ).

CR 2032 coin cells were assembled in a glove box using the prepared air cathode, lithium foil as the anode, a Whatman glass fiber (GF/A) separator, and a 1 M LiTFSI TEGDME (tetraethylene glycol dimethyl ether) electrolyte. The assembled cell was allowed to rest for 12 h in an air atmosphere before conducting discharge-charge tests. The discharge-charge tests (Neware BTS 8.0, Neware, Dongguan, China) were carried out in the constant current (CC) mode under flowing air gas (60 sccm), and the cut-off voltage was set to a range from 2.2 V to 4.5 V at 200 mA·g<sup>-1</sup> and 500 mA·g<sup>-1</sup>.

Galvanostatic discharge-charge profiles were collected using the same battery cycler. To gain a more comprehensive understanding of the electrochemical responses of all cathodes, electrochemical impedance spectroscopy (EIS) was also conducted at an amplitude of 0.01 V, and a frequency range of 1 MHz to 0.01 Hz of the LABs was also applied to evaluate the LABs performances.

## 3. Results and Discussion

### 3.1. Characterization of Samples

Figure 1 presents the TGA measurement values of different samples. While NiCo<sub>2</sub>O<sub>4</sub> remains relatively stable up to temperatures exceeding 800 °C, it can be observed that both MWCNTs-COOH and NiCo<sub>2</sub>O<sub>4</sub>@CNTs experience a rapid combustion of carbon at temperatures exceeding 350 °C, causing it to dissipate. Specifically, when calculating the evaporation rate of NiCo<sub>2</sub>O<sub>4</sub>@CNTs, carbon was found to account for approximately 8%. This implies that the synthesized NiCo<sub>2</sub>O<sub>4</sub>@CNTs composites contained a CNT content of 8%.

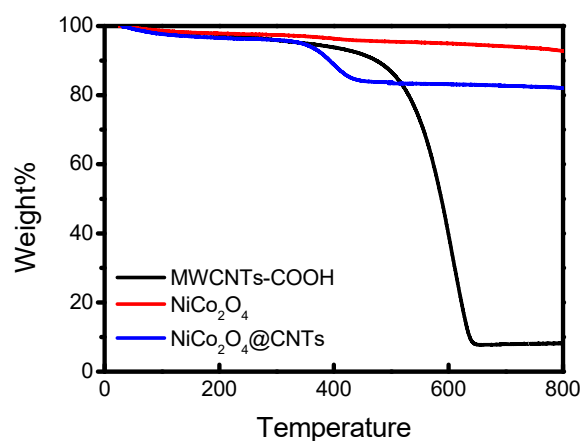


Figure 1. TGA curves of the different samples.

Figure 2 shows the EDS mapping image of the NiCo<sub>2</sub>O<sub>4</sub>@CNTs composites. This was performed to experimentally analyze the components more accurately. Table 1 presents the mass and atomic ratios of the NiCo<sub>2</sub>O<sub>4</sub>@CNTs composites. When examining the chart, it is clear that each element is visibly distributed. The composite contains 21.21% carbon, 37.48% oxygen, 28.93% cobalt, and 12.37% nickel. While EDS mapping does not provide a quantitative distribution, it still confirms that the elements coexist in a granular form through the synthesis. These results confirm that the synthesis was successfully achieved.

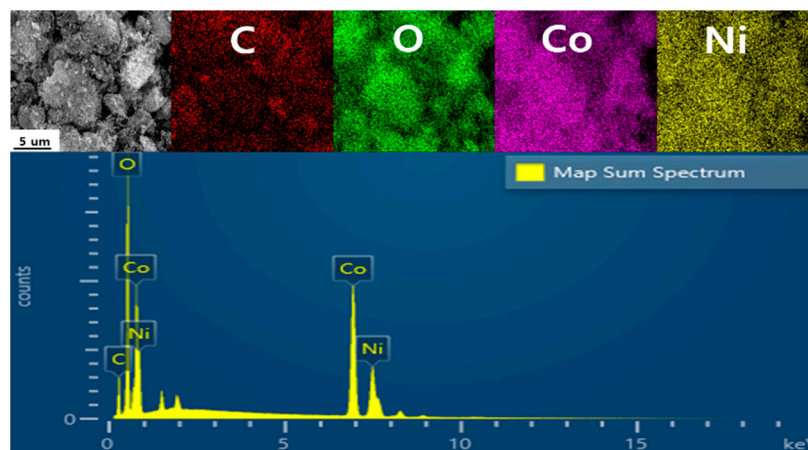


Figure 2. EDS mapping of the  $\text{NiCo}_2\text{O}_4@\text{CNTs}$  composites.

Table 1. EDS mapping data of the obtained  $\text{NiCo}_2\text{O}_4@\text{CNTs}$  composites.

Element	Wt %	Atomic %
C	21.21	36.71
O	37.48	48.70
Co	28.93	10.21
Ni	12.37	4.38
Total	99.99	100

Figure 3 presents the X-ray diffraction analysis (XRD), which was conducted to analyze the structural characteristics of the  $\text{NiCo}_2\text{O}_4@\text{CNTs}$  composites and other samples. The pattern of the  $\text{NiCo}_2\text{O}_4@\text{CNTs}$  closely matches that of  $\text{NiCo}_2\text{O}_4$ , with a slight presence of the MWCNTs pattern. In the XRD pattern of the MWCNTs-COOH, the two peaks at  $25.9^\circ$  and  $43^\circ$  correspond to the (002) and (100) planes, respectively, and the peaks at  $18.90^\circ$ ,  $31.14^\circ$ ,  $36.69^\circ$ ,  $44.62^\circ$ ,  $59.09^\circ$ , and  $64.98^\circ$  are respectively identified as the (111), (220), (311), (400), (511), and (440) planes belonging to the  $\text{NiCo}_2\text{O}_4$ , and the  $\text{NiCo}_2\text{O}_4@\text{CNTs}$  pattern contains both samples. No additional impurities or peaks corresponding to other phases were observed.

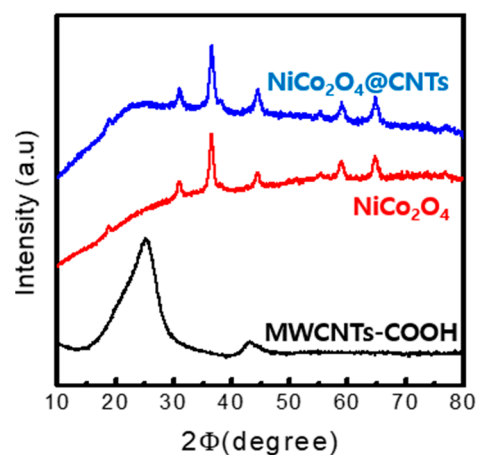
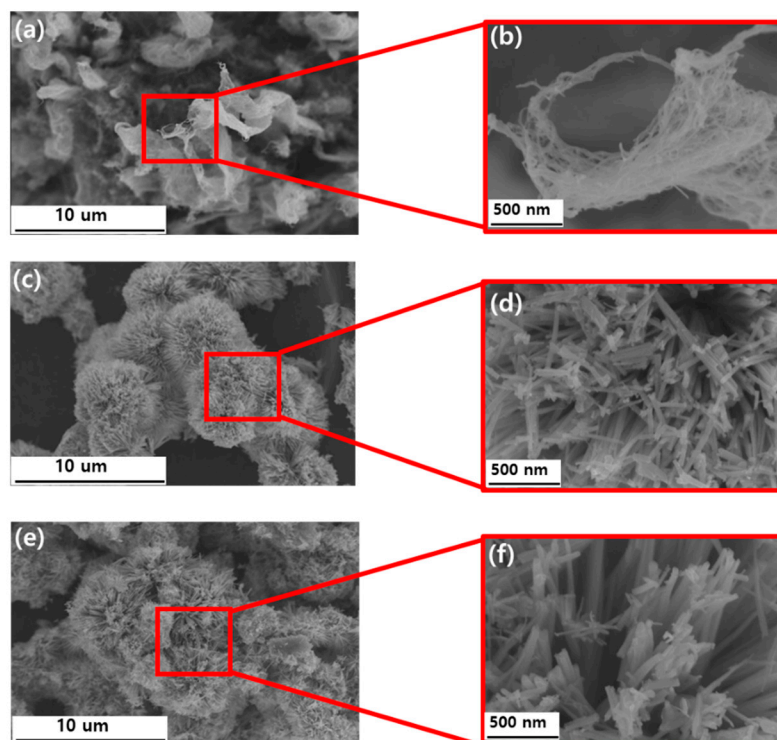


Figure 3. XRD patterns of different samples.

Figure 4 shows an SEM image taken to examine the morphologies of the MWCNTs-COOH,  $\text{NiCo}_2\text{O}_4$ , and  $\text{NiCo}_2\text{O}_4@\text{CNTs}$ . Figure 4a,b depict MWCNT-COOH with a smooth-walled structure. Figure 4c,d show the images of  $\text{NiCo}_2\text{O}_4$ . Upon inspection of the images, it can be observed that spherical structures resembling needles have formed. Figure 4e,f

show the presence of CNTs alongside the nanoneedle cluster structures. While the majority of the morphology corresponds to  $\text{NiCo}_2\text{O}_4$ , the content of CNTs has been previously investigated using EDS mapping and TGA.



**Figure 4.** SEM image of MWCNTs-COOH (a,b),  $\text{NiCo}_2\text{O}_4$  (c,d), and  $\text{NiCo}_2\text{O}_4$ @CNTs composites (e,f).

$\text{N}_2$  adsorption-desorption isotherms of the different samples are compiled in Figure 5 for the analysis of their porous structure, revealing a large surface area. The numerical values for each sample are presented in Table 2. The surface area value of MWCNTs-COOH is  $417.53 \text{ m}^2 \cdot \text{g}^{-1}$  and that of  $\text{NiCo}_2\text{O}_4$  is  $100.83 \text{ m}^2 \cdot \text{g}^{-1}$ . The specific surface area value of  $\text{NiCo}_2\text{O}_4$ @CNTs ( $221.21 \text{ m}^2 \cdot \text{g}^{-1}$ ) falls between the values of the other two samples, as observed. This once again demonstrates the successful outcome of the previous synthesis experiment for  $\text{NiCo}_2\text{O}_4$ @CNTs.

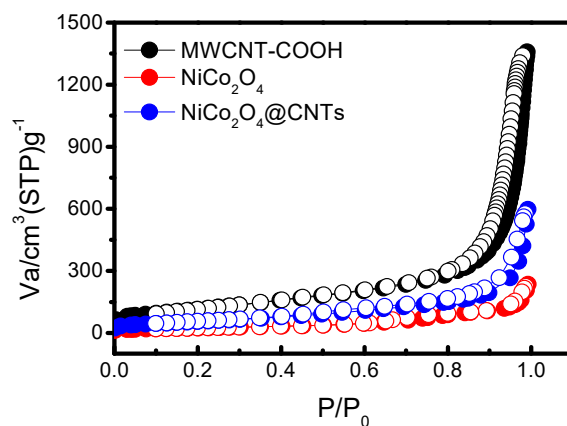


**Figure 5.**  $\text{N}_2$  adsorption-desorption isotherm plots of different samples.

Surface area is one of the critical factors of anode performance. If it is too large, capacity may be limited [39–41]. This is, in part, attributed to the binder, which blocks most

pores below  $\sim 300 \text{ \AA}$ , and which is a dominant influence on the pore-size distribution for many high-surface-area carbons.

**Table 2.**  $\text{N}_2$  adsorption-desorption representing the surface area.

Sample	S ( $\text{m}^2 \cdot \text{g}^{-1}$ )
MWCNTs-COOH	417.53
$\text{NiCo}_2\text{O}_4$	100.83
$\text{NiCo}_2\text{O}_4@\text{CNTs}$	221.21

### 3.2. Electrochemical Performance

Figure 6 illustrates the electrochemical impedance spectroscopy (EIS) data for each assessed cathode, evaluated on LABs at an open circuit voltage (OCV) over a range of frequencies from 1 MHz to 0.01 Hz, with an amplitude of 0.01 V. The depressed semicircle in the middle of the frequency range represents the charge transfer resistance ( $R_{ct}$ ), which can be evaluated using the diameter of the semicircle [42,43]. The  $R_{ct}$  of the MWCNTs-COOH,  $\text{NiCo}_2\text{O}_4$ , and  $\text{NiCo}_2\text{O}_4@\text{CNTs}$  cathodes were 279  $\Omega$ , 281  $\Omega$ , and 211  $\Omega$ , respectively, indicating that the transfer resistance of the  $\text{NiCo}_2\text{O}_4@\text{CNTs}$  before recharging was smaller than those of MWCNTs-COOH and  $\text{NiCo}_2\text{O}_4$  cathodes. From the results, it can be inferred that the low transfer resistance of the  $\text{NiCo}_2\text{O}_4@\text{CNTs}$  may contribute to the outstanding reversibility of ORR and OER and the enhancement in electrochemical performance.

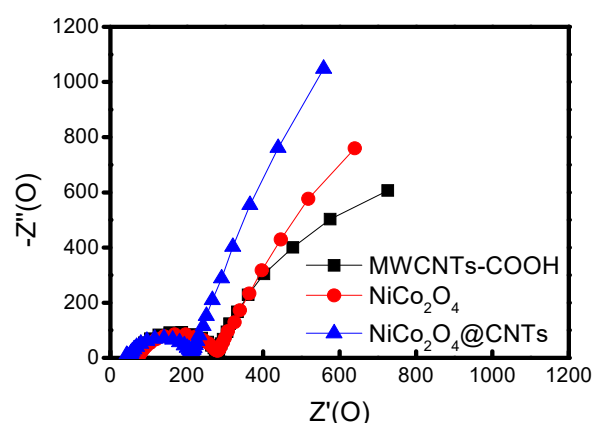


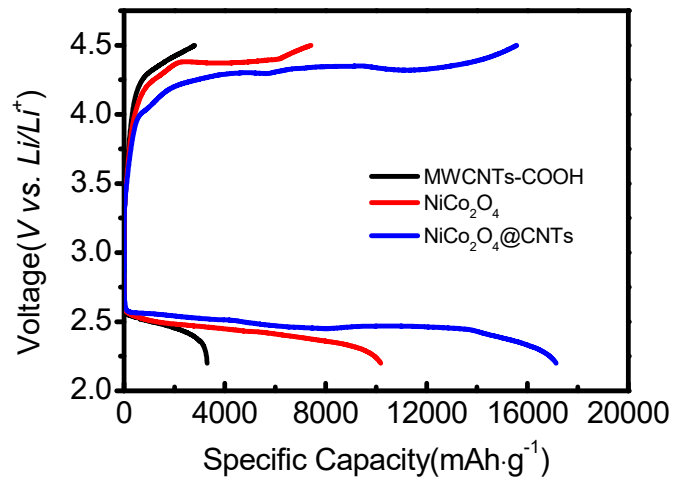
**Figure 6.** EIS spectra of different electrode cells before recharge.

The coin cells assembled using the prepared samples underwent discharge-charge testing in an air atmosphere within a voltage range of 2.2 to 4.5 V. Figure 7 presents the first galvanostatic discharge and charge profiles of the different electrodes at a current density of  $400 \text{ mA} \cdot \text{g}^{-1}$  from 2.2 to 4.5 V. As a result, the discharge specific capacities of the MWCNTs-COOH,  $\text{NiCo}_2\text{O}_4$ , and  $\text{NiCo}_2\text{O}_4@\text{CNTs}$  cathodes were 3,297, 10,180, and 17,137  $\text{mAh} \cdot \text{g}^{-1}$ , respectively. Specifically, the specific capacity of MWCNTs-COOH was measured to be relatively lower, which is believed to be attributed to the discharge byproducts ( $\text{Li}_2\text{O}_2$ ) formed during the discharge-charge process, obstructing active sites and resulting in reduced capacity.

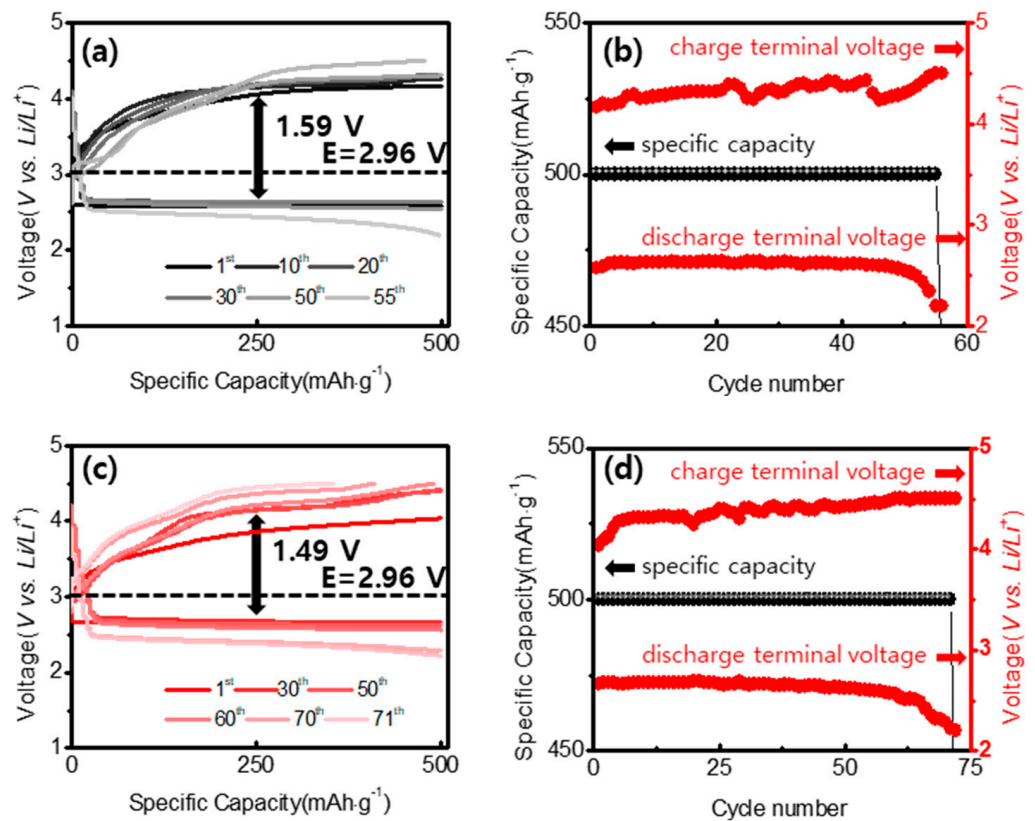
The addition of catalysts substantially increased the discharge-specific capacity and overall performance of the coin cells [44]. This discovery confirms that the porous and heterostructured design of  $\text{NiCo}_2\text{O}_4$  electrodes provides more space and sites for the accumulation of  $\text{Li}^+$  ions, leading to improved energy storage performance compared to other electrodes.

The current density testing was conducted under conditions of  $200 \text{ mA} \cdot \text{g}^{-1}$  and  $500 \text{ mA} \cdot \text{g}^{-1}$ , and the capacity was set at  $500 \text{ mAh} \cdot \text{g}^{-1}$ . Both the current density and capacity were determined based on the combined values of the carbon and metal oxides. The voltage gap is the difference between the charge terminal voltage point and the discharge

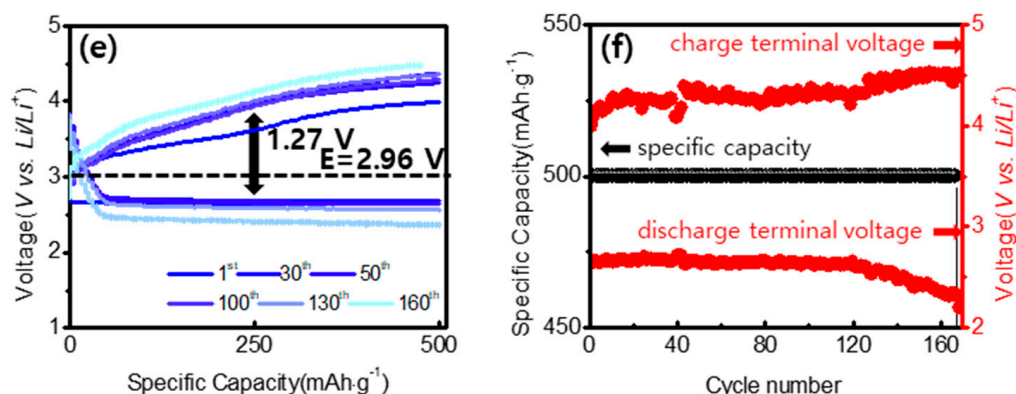
terminal voltage point after the 30th cycle. Figure 8 shows the discharge-charge process under a limited capacity mode of  $500 \text{ mAh}\cdot\text{g}^{-1}$  at a specific current of  $200 \text{ mA}\cdot\text{g}^{-1}$ . Figure 8a,b represent the discharge-charge cycle curves of the MWCNTs-COOH. It can be observed that approximately 55 cycles of charge and discharge occur, after which the capacity was no longer maintained. The electrode also showed quite large voltage gaps of  $1.59 \text{ V}$  (Figure 8a) at 30 cycles. Therefore, it is evident that in cells using only carbon, discharge-charge cycles occur relatively briefly. The reason for this is that discharge byproducts ( $\text{Li}_2\text{O}_2$ ) on the air cathode do not decompose and accumulate and obstruct active sites.



**Figure 7.** Comparison of the initial discharge-charge profiles of the LABs from 2.2 to 4.5 V for MWCNTs-COOH,  $\text{NiCo}_2\text{O}_4$ , and  $\text{NiCo}_2\text{O}_4@\text{CNTs}$  cathode at  $400 \text{ mA}\cdot\text{g}^{-1}$ .



**Figure 8.** Cont.



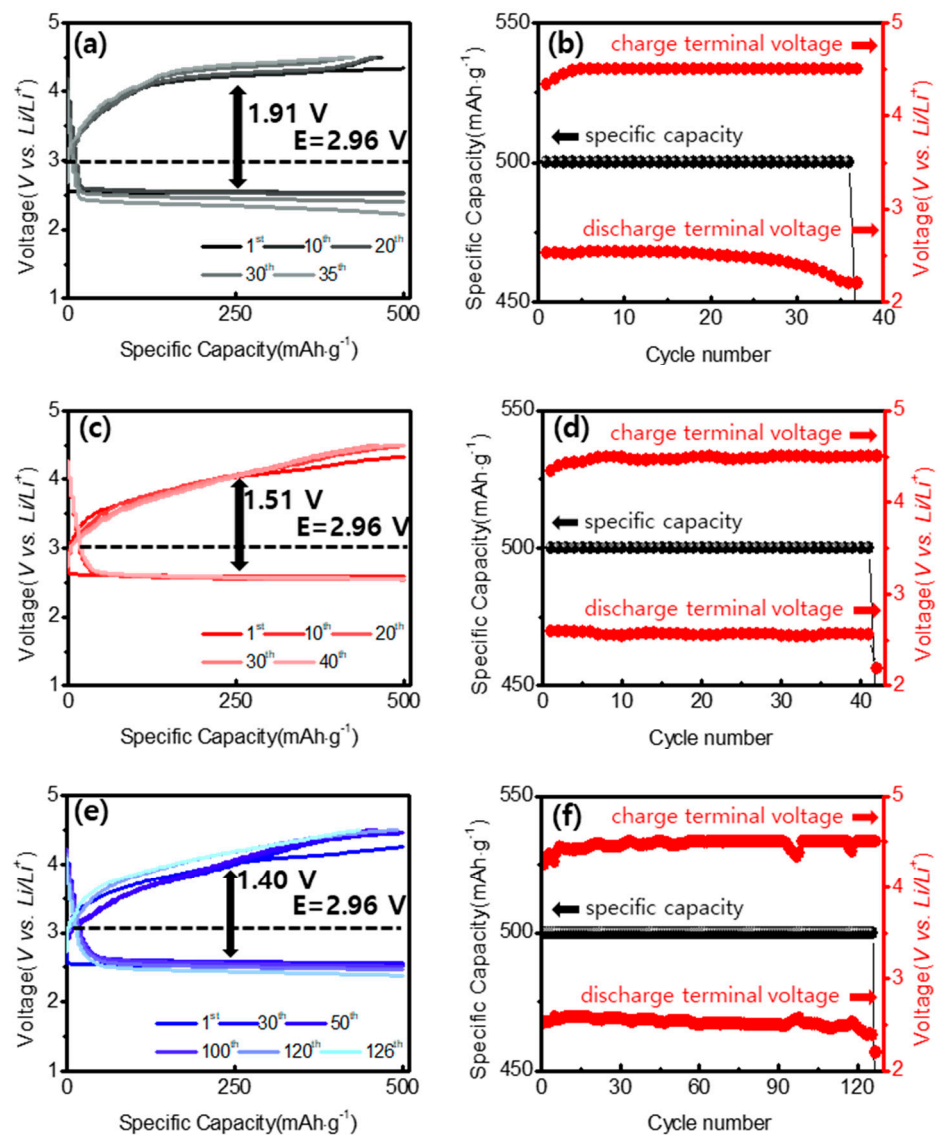
**Figure 8.** (a) Galvanostatic discharge-charge voltage MWCNTs-COOH and (b) voltages corresponding to (a). (c) Galvanostatic discharge-charge voltage  $\text{NiCo}_2\text{O}_4$  and (d) voltages corresponding to (c). (e) Galvanostatic discharge-charge voltage  $\text{NiCo}_2\text{O}_4@\text{CNTs}$  and (f) voltages corresponding to (e) at a current density of  $200 \text{ mA}\cdot\text{g}^{-1}$ .

Figure 8c,d depict the  $\text{NiCo}_2\text{O}_4$  samples, which maintained cycling for approximately 71 cycles. The electrode showed voltage gaps of 1.49 V (Figure 8c) at 30 cycles. This indicates that it has better performance characteristics than MWCNT-COOH. Figure 8e,f depict the cycling characteristics of the  $\text{NiCo}_2\text{O}_4@\text{CNTs}$  composite. It maintained its capacity for approximately 160 cycles, demonstrating significantly higher cycling stability compared to other samples. The electrode showed quite low voltage gaps of 1.27 V (Figure 8e) at 30 cycles. This was the lowest voltage value among the samples.

As demonstrated in our experiments, the  $\text{NiCo}_2\text{O}_4@\text{CNTs}$  composite with an appropriate carbon content significantly enhanced electrochemical performance [45]. Notably, the ultrahigh electrochemical performance of the  $\text{NiCo}_2\text{O}_4@\text{CNTs}$  composite can be attributed to its unique three-dimensional structure [46,47]. During the formation of the nanoneedle cluster cathode structure, more active sites were created on the surface, improving OER and ORR performance and thereby enhancing the effective activity of the catalyst. However, pure  $\text{NiCo}_2\text{O}_4$  exhibited relatively low cycle stability due to its very low specific surface area, resulting in a limited number of active sites. For a more thorough evaluation of cyclability at a high specific current, the coin cells were also evaluated at a specific current of  $500 \text{ mA}\cdot\text{g}^{-1}$  (Figure 9). It was surprising that even at such an elevated discharge-charge rate, the cell with the  $\text{NiCo}_2\text{O}_4@\text{CNTs}$  composite performed for 120 cycles, while the cells containing the MWCNTs-COOH and  $\text{NiCo}_2\text{O}_4$  cells operated for only 35 and 42 cycles. This confirms that there is a distinct difference in cycle stability, particularly as the current density increases. In particular,  $\text{NiCo}_2\text{O}_4@\text{CNTs}$  composites exhibited significantly higher cycle characteristics compared to the other two samples.

The  $\text{NiCo}_2\text{O}_4@\text{CNTs}$  composite electrode also showed quite low voltage gaps of 1.40 V (Figure 9e) at 30 cycles among all samples. The  $\text{NiCo}_2\text{O}_4@\text{CNTs}$  not only provided a straightforward pathway for electron transport but also aided in the decomposition of  $\text{Li}_2\text{CO}_3$  and  $\text{Li}_2\text{O}_2$ , helping to reduce over-potentials and ultimately leading to stability.

Figure 10 presents the surface after the fifth discharge-charge cycle ( $500 \text{ mA}\cdot\text{g}^{-1}$ ,  $500 \text{ mAh}\cdot\text{g}^{-1}$ ) for MWCNTs,  $\text{NiCo}_2\text{O}_4$ , and  $\text{NiCo}_2\text{O}_4@\text{CNTs}$ . Figure 10a represents MWCNTs-COOH. Upon examining the images, it is evident that discharge byproducts ( $\text{Li}_2\text{O}_2$ ) generated during the charge-discharge process are not decomposed and remain abundantly on the surface. Figure 10b represents the surface of  $\text{NiCo}_2\text{O}_4$ . It is observed that the decomposition of discharge byproducts on the surface of  $\text{NiCo}_2\text{O}_4$  occurred more effectively than in MWCNTs-COOH. This can be interpreted as a well-supported catalytic role. Finally, Figure 10c depicts the composite of  $\text{NiCo}_2\text{O}_4@\text{CNTs}$ . The image in Figure 10c confirms that the decomposition of  $\text{Li}_2\text{O}_2$  most effectively occurs on the surface of  $\text{NiCo}_2\text{O}_4@\text{CNTs}$ . This indicates excellent cycle stability through the most reversible reaction.



**Figure 9.** (a) Galvanostatic discharge-charge voltage MWCNTs-COOH and (b) voltages corresponding to (a). (c) Galvanostatic discharge-charge voltage NiCo<sub>2</sub>O<sub>4</sub> and (d) voltages corresponding to (c). (e) Galvanostatic discharge-charge voltage NiCo<sub>2</sub>O<sub>4</sub>@CNTs and (f) voltages corresponding to (e) at a current density of 500 mA·g<sup>-1</sup>.

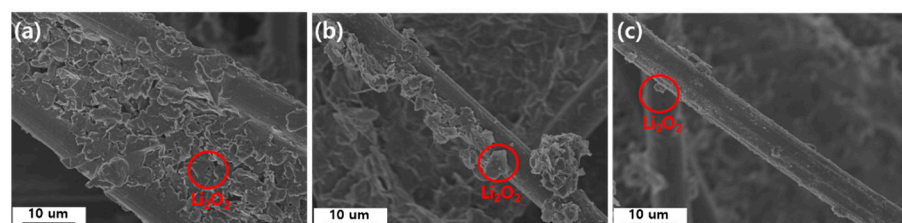


**Figure 10.** SEM images of (a) MWCNTs-COOH, (b) NiCo<sub>2</sub>O<sub>4</sub>, and (c) NiCo<sub>2</sub>O<sub>4</sub>@CNTs after 5th charging.

Figure 11 shows the rate performance of the NiCo<sub>2</sub>O<sub>4</sub>@CNTs composite. The current densities progressively increased from 50 to 100, 200, 300, and 500 mA·g<sup>-1</sup>. No notable increase in polarization was observed in the discharging processes; in contrast, the charge polarization increased gradually, especially at current densities of 300 mA·g<sup>-1</sup> and 500 mA g<sup>-1</sup>. This indicates a gradual decrease in cycle performance from a current density of 300 mA·g<sup>-1</sup>. Therefore, as the current density increases, the cycle life characteristics

decrease accordingly. The NiCo<sub>2</sub>O<sub>4</sub>@CNTs electrode displayed a great rate of performance in lithium-air batteries. These results confirm superior performance compared to cycle life and capacity data reported in other papers with different catalysts on CNTs [48,49].

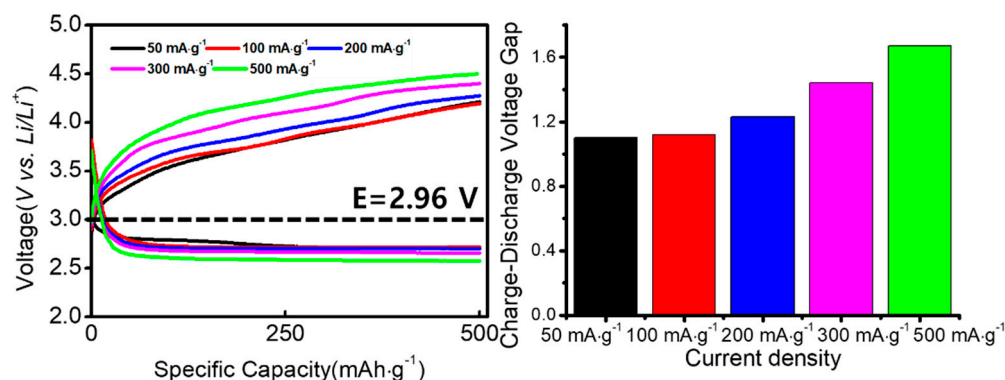


**Figure 11.** Cell potential profiles of the Li-air cells using NiCo<sub>2</sub>O<sub>4</sub>@CNTs composites at different current densities.

Figure 12 illustrates a schematic of the discharge-charge process of the NiCo<sub>2</sub>O<sub>4</sub>@CNTs. In such a unique structure, the ultrafine NiCo<sub>2</sub>O<sub>4</sub> phase offered high catalytic activity for ORR and OER. However, in this document, the studied catalyst, NiCo<sub>2</sub>O<sub>4</sub>, had a spherical shape with a reported surface area of 90 m<sup>2</sup>·g<sup>-1</sup> [50]. In contrast, we achieved a nanoneedle cluster structure with a surface area of 221.21 m<sup>2</sup>·g<sup>-1</sup>. This study suggests that the NiCo<sub>2</sub>O<sub>4</sub>@CNTs we synthesized significantly expanded the active site area, resulting in high-performance characteristics within the catalyst material itself. As a whole, these electrochemical performance results make the NiCo<sub>2</sub>O<sub>4</sub>@CNTs composite a promising candidate for LABs.

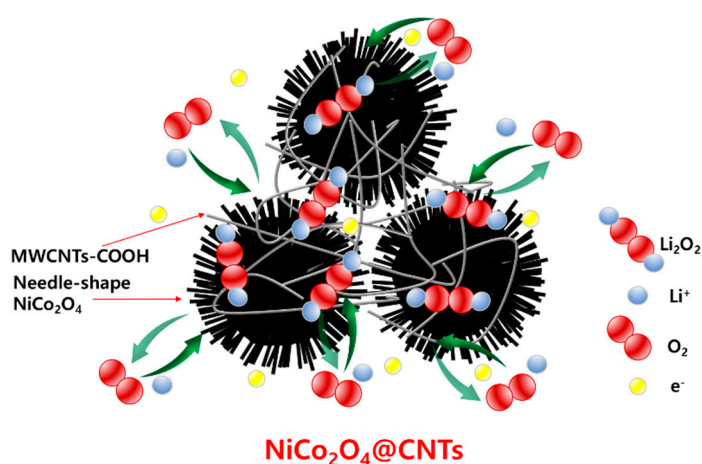


**Figure 12.** Schematic illustration of the discharge-charge process of NiCo<sub>2</sub>O<sub>4</sub>@CNTs composite electrodes.

#### 4. Conclusions

In this study, MWCNTs-COOH, NiCo<sub>2</sub>O<sub>4</sub>, and NiCo<sub>2</sub>O<sub>4</sub>@CNTs were synthesized and prepared using hydrothermal synthesis and sintering processes. Subsequently, material analysis and electrochemical evaluations were conducted. Initially, TGA measurements confirmed an 8% carbon content in the NiCo<sub>2</sub>O<sub>4</sub>@CNTs, and EDS mapping was utilized to determine the composite's composition ratio. Further structural analysis was carried out using XRD, while morphological analysis was conducted using SEM. BET measurements revealed that the specific surface area of the NiCo<sub>2</sub>O<sub>4</sub>@CNTs at 221.21 m<sup>2</sup>·g<sup>-1</sup> represented an intermediate value between the other two samples. The resulting NiCo<sub>2</sub>O<sub>4</sub>@CNTs composites were successfully designed and applied as the air cathode for a Li-air battery,

and an electrochemical evaluation test was conducted. First, EIS measurements revealed a significant reduction in charge transfer resistance for the NiCo<sub>2</sub>O<sub>4</sub>@CNTs cell. The battery utilizing the NiCo<sub>2</sub>O<sub>4</sub>@CNTs composite air cathode demonstrated stable cycling performance for more than 100 cycles at current densities of 200 mA·g<sup>-1</sup> and 500 mA·g<sup>-1</sup>. The NiCo<sub>2</sub>O<sub>4</sub>@CNTs composite air electrode revealed two times longer lifespan with 1.27 V (200 mA·g<sup>-1</sup>) and 1.40 V (500 mA·g<sup>-1</sup>) lower over-potentials. To analyze this, the surface of the electrode was examined after 30 cycles, revealing that NiCo<sub>2</sub>O<sub>4</sub>@CNTs composites promote the decomposition of discharge byproducts (Li<sub>2</sub>O<sub>2</sub>). The cell exhibited very great stability after extended cycles in air, avoiding the instability issues of conventional non-aqueous Li-air batteries. Overall, this study confirms the feasibility of enhanced designs for air cathodes in Li-air batteries.

**Author Contributions:** Conceptualization, D.-S.H.; Formal analysis, Y.-J.C., C.-S.J., K.-H.S. and W.-J.S.; Writing—review & editing, S.-H.Y. All authors have read and agreed to the published version of the manuscript.

**Funding:** This research was supported by a grant from the R&D Program (20220610100010, 20023127) funded by the Ministry of Trade, Industry and Energy, and the R&D Program (C3-2410, C3-2426, C3-2411) funded by the KIER of Republic of Korea, respectively.

**Data Availability Statement:** Data are contained within the article.

**Conflicts of Interest:** The authors declare no conflict of interest.

## References

1. Liu, T.; Vivek, J.P.; Zhao, E.W.; Lei, J.; Garcia-Araez, N.; Grey, C.P. Current Challenges and Routes Forward for Nonaqueous Lithium-Air Batteries. *Chem. Rev.* **2020**, *120*, 6558–6625. [[CrossRef](#)] [[PubMed](#)]
2. Nam, J.S.; Jung, J.W.; Youn, D.Y.; Cho, S.H.; Cheong, J.Y.; Kim, M.S.; Song, S.W.; Kim, S.J.; Kim, I.D. Free-Standing Carbon Nanofibers Protected by a Thin Metallic Iridium Layer for Extended Life-Cycle Li-Oxygen Batteries. *ACS Appl. Mater. Interfaces* **2020**, *12*, 55756–55765. [[CrossRef](#)] [[PubMed](#)]
3. Liu, Y.J.; He, P.; Zhou, H.S. Rechargeable Solid-State Li-Air and Li-S Batteries: Materials, Construction, and Challenges. *Adv. Energy Mater.* **2018**, *8*, 1701602. [[CrossRef](#)]
4. Li, J.L.; Daniel, C.; Wood, D. Materials processing for lithium-ion batteries. *J. Power Sources* **2011**, *196*, 2452–2460. [[CrossRef](#)]
5. Schmich, R.; Wagner, R.; Horpel, G.; Placke, T.; Winter, M. Performance and cost of materials for lithium-based rechargeable automotive batteries. *Nat. Energy* **2018**, *3*, 267–278. [[CrossRef](#)]
6. Yadegari, H.; Sun, Q.; Sun, X.L. Sodium-Oxygen Batteries: A Comparative Review from Chemical and Electrochemical Fundamentals to Future Perspective. *Adv. Mater.* **2016**, *28*, 7065–7093. [[CrossRef](#)] [[PubMed](#)]
7. Shao, Y.Y.; Park, S.; Xiao, J.; Zhang, J.G.; Wang, Y.; Liu, J. Electrocatalysts for Nonaqueous Lithium-Air Batteries: Status, Challenges, and Perspective. *Acs Catal.* **2012**, *2*, 844–857. [[CrossRef](#)]
8. Shao, Y.Y.; Ding, F.; Xiao, J.; Zhang, J.; Xu, W.; Park, S.; Zhang, J.G.; Wang, Y.; Liu, J. Making Li-Air Batteries Rechargeable: Material Challenges. *Adv. Funct. Mater.* **2013**, *23*, 987–1004. [[CrossRef](#)]
9. Grande, L.; Paillard, E.; Hassoun, J.; Park, J.B.; Lee, Y.J.; Sun, Y.K.; Passerini, S.; Scrosati, B. The Lithium/Air Battery: Still an Emerging System or a Practical Reality? *Adv. Mater.* **2015**, *27*, 784–800. [[CrossRef](#)]
10. Aurbach, D.; McCloskey, B.D.; Nazar, L.F.; Bruce, P.G. Advances in understanding mechanisms underpinning lithium-air batteries. *Nat. Energy* **2016**, *1*, 16128. [[CrossRef](#)]
11. Sennu, P.; Park, H.S.; Park, K.U.; Aravindan, V.; Nahm, K.S.; Lee, Y.S. Formation of NiCo<sub>2</sub>O<sub>4</sub> rods over Co<sub>3</sub>O<sub>4</sub> nanosheets as efficient catalyst for Li-O<sub>2</sub> batteries and water splitting. *J. Catal.* **2017**, *349*, 175–182. [[CrossRef](#)]
12. Abraham, K.M.; Jiang, Z. A polymer electrolyte-based rechargeable lithium/oxygen battery. *J. Electrochem. Soc.* **1996**, *143*, 1. [[CrossRef](#)]
13. Débart, A.; Paterson, A.J.; Bao, J.; Bruce, P.G.  $\alpha$ -MnO<sub>2</sub> nanowires: A catalyst for the O<sub>2</sub> electrode in rechargeable lithium batteries. *Angew. Chem.-Int. Ed.* **2008**, *47*, 4521–4524. [[CrossRef](#)] [[PubMed](#)]
14. Laoire, C.O.; Mukerjee, S.; Abraham, K.M.; Plichta, E.J.; Hendrickson, M.A. Elucidating the Mechanism of Oxygen Reduction for Lithium-Air Battery Applications. *J. Phys. Chem. C* **2009**, *113*, 20127–20134. [[CrossRef](#)]
15. Li, F.J.; Ohnishi, R.; Yamada, Y.; Kubota, J.; Domen, K.; Yamada, A.; Zhou, H.S. Carbon supported TiN nanoparticles: An efficient bifunctional catalyst for non-aqueous LiO<sub>2</sub> batteries. *Chem. Commun.* **2013**, *49*, 1175–1177. [[CrossRef](#)] [[PubMed](#)]
16. Ma, Z.; Yuan, X.X.; Li, L.; Ma, Z.F.; Wilkinson, D.P.; Zhang, L.; Zhang, J.J. A review of cathode materials and structures for rechargeable lithium-air batteries. *Energy Environ. Sci.* **2015**, *8*, 2144–2198. [[CrossRef](#)]

17. Li, Y.; Zou, L.L.; Li, J.; Guo, K.; Dong, X.W.; Li, X.W.; Xue, X.Z.; Zhang, H.F.; Yang, H. Synthesis of ordered mesoporous NiCo<sub>2</sub>O<sub>4</sub> via hard template and its application as bifunctional electrocatalyst for LiO<sub>2</sub> batteries. *Electrochim. Acta* **2014**, *129*, 14–20. [[CrossRef](#)]
18. Zhang, L.L.; Zhang, F.F.; Huang, G.; Wang, J.W.; Du, X.C.; Qin, L.; Wang, L.M. Freestanding MnO<sub>2</sub>@carbon papers air electrodes for rechargeable LiO<sub>2</sub> batteries. *J. Power Sources* **2014**, *261*, 311–316. [[CrossRef](#)]
19. Hu, X.F.; Wang, J.B.; Li, T.F.; Wang, J.Q.; Gregory, D.H.; Chen, J. MCNTs@MnO<sub>2</sub> Nanocomposite Cathode Integrated with Soluble O-2-Carrier Co-salen in Electrolyte for High-Performance Li-Air Batteries. *Nano Lett.* **2017**, *17*, 2073–2078. [[CrossRef](#)]
20. Girishkumar, G.; McCloskey, B.; Luntz, A.C.; Swanson, S.; Wilcke, W. Lithium—Air Battery: Promise and Challenges. *J. Phys. Chem. Lett.* **2010**, *1*, 2193–2203. [[CrossRef](#)]
21. Tan, P.; Jiang, H.R.; Zhu, X.B.; An, L.; Jung, C.Y.; Wu, M.C.; Shi, L.; Shyy, W.; Zhao, T.S. Advances and challenges in lithium-air batteries. *Appl. Energy* **2017**, *204*, 780–806. [[CrossRef](#)]
22. Lee, J.H.; Black, R.; Popov, G.; Pomerantseva, E.; Nan, F.H.; Botton, G.A.; Nazar, L.F. The role of vacancies and defects in Na<sub>0.44</sub>MnO<sub>2</sub> nanowire catalysts for lithium-oxygen batteries. *Energy Environ. Sci.* **2012**, *5*, 9558–9565. [[CrossRef](#)]
23. Lu, Y.C.; Gallant, B.M.; Kwabi, D.G.; Harding, J.R.; Mitchell, R.R.; Whittingham, M.S.; Shao-Horn, Y. Lithium-oxygen batteries: Bridging mechanistic understanding and battery performance. *Energy Environ. Sci.* **2013**, *6*, 750–768. [[CrossRef](#)]
24. Ban, J.J.; Xu, H.J.; Cao, G.Q.; Fan, Y.M.; Pang, W.K.; Shao, G.S.; Hu, J.H. Synergistic Effects of Phase Transition and Electron-Spin Regulation on the Electrocatalysis Performance of Ternary Nitride. *Adv. Funct. Mater.* **2023**, *33*, 2300623. [[CrossRef](#)]
25. Liu, Y.; Cao, L.J.; Cao, C.W.; Wang, M.; Leung, K.L.; Zeng, S.S.; Hung, T.F.; Chung, C.Y.; Lu, Z.G. Facile synthesis of spinel CuCo<sub>2</sub>O<sub>4</sub> nanocrystals as high-performance cathode catalysts for rechargeable Li-air batteries. *Chem. Commun.* **2014**, *50*, 14635–14638. [[CrossRef](#)] [[PubMed](#)]
26. Umeshbabu, E.; Rajeshkhanna, G.; Justin, P.; Rao, G.R. Magnetic, optical and electrocatalytic properties of urchin and sheaf-like NiCo<sub>2</sub>O<sub>4</sub> nanostructures. *Mater. Chem. Phys.* **2015**, *165*, 235–244. [[CrossRef](#)]
27. Umeshbabu, E.; Rajeshkhanna, G.; Rao, G.R. Urchin and sheaf-like NiCo<sub>2</sub>O<sub>4</sub> nanostructures: Synthesis and electrochemical energy storage application. *Int. J. Hydrogen Energy* **2014**, *39*, 15627–15638. [[CrossRef](#)]
28. Yuan, C.Z.; Li, J.Y.; Hou, L.R.; Zhang, X.G.; Shen, L.F.; Lou, X.W. Ultrathin Mesoporous NiCo<sub>2</sub>O<sub>4</sub> Nanosheets Supported on Ni Foam as Advanced Electrodes for Supercapacitors. *Adv. Funct. Mater.* **2012**, *22*, 4592–4597. [[CrossRef](#)]
29. Shi, H.J.; Zhao, G.H. Water Oxidation on Spinel NiCo<sub>2</sub>O<sub>4</sub> Nanoneedles Anode: Microstructures, Specific Surface Character, and the Enhanced Electrocatalytic Performance. *J. Phys. Chem. C* **2014**, *118*, 25939–25946. [[CrossRef](#)]
30. Chen, R.; Wang, H.Y.; Miao, J.W.; Yang, H.B.; Liu, B. A flexible high-performance oxygen evolution electrode with three-dimensional NiCo<sub>2</sub>O<sub>4</sub> core-shell nanowires. *Nano Energy* **2015**, *11*, 333–340. [[CrossRef](#)]
31. Shi, X.; Bernasek, S.L.; Selloni, A. Oxygen Deficiency and Reactivity of Spinel NiCo<sub>2</sub>O<sub>4</sub> (001) Surfaces. *J. Phys. Chem. C* **2017**, *121*, 3929–3937. [[CrossRef](#)]
32. Yattoo, M.A.; Seymour, I.D.; Skinner, S.J. Neutron diffraction and DFT studies of oxygen defect and transport in higher-order Ruddlesden-Popper phase materials. *Rsc Adv.* **2023**, *13*, 13786–13797. [[CrossRef](#)] [[PubMed](#)]
33. Zhang, J.W.; Zhang, L.L.; Zhang, J.W.; Zhang, Z.J.; Wu, Z.S. Effect of surface/bulk oxygen vacancies on the structure and electrochemical performance of TiO<sub>2</sub> nanoparticles. *J. Alloys Compd.* **2015**, *642*, 28–33. [[CrossRef](#)]
34. Wen, Z.Y.; Shen, C.; Lu, Y. Air Electrode for the Lithium-Air Batteries: Materials and Structure Designs. *Chempluschem* **2015**, *80*, 270–287. [[CrossRef](#)]
35. Jin, S.; Jiang, Y.; Ji, H.X.; Yu, Y. Advanced 3D Current Collectors for Lithium-Based Batteries. *Adv. Mater.* **2018**, *30*, 1802014. [[CrossRef](#)] [[PubMed](#)]
36. Zheng, Y.J.; Lin, Z.Q.; Chen, W.J.; Liang, B.H.; Du, H.W.; Yang, R.L.; He, X.F.; Tang, Z.K.; Gui, X.C. Flexible, sandwich-like CNTs/NiCo<sub>2</sub>O<sub>4</sub> hybrid paper electrodes for all-solid state supercapacitors. *J. Mater. Chem. A* **2017**, *5*, 5886–5894. [[CrossRef](#)]
37. Gao, S.W.; Sui, Y.W.; Wei, F.X.; Qi, J.Q.; Meng, Q.K.; He, Y.Z. Facile synthesis of cuboid Ni-MOF for high-performance supercapacitors. *J. Mater. Sci.* **2018**, *53*, 6807–6818. [[CrossRef](#)]
38. Kumar, N.; Yu, Y.C.; Lu, Y.H.; Tseng, T.Y. Fabrication of carbon nanotube/cobalt oxide nanocomposites via electrophoretic deposition for supercapacitor electrodes. *J. Mater. Sci.* **2016**, *51*, 2320–2329. [[CrossRef](#)]
39. Younesi, R.; Singh, N.; Urbonaitis, S.; Edström, K. The Effect of Pore Size on the Performance of the LiO<sub>2</sub> Battery. In Proceedings of the Symposium on Battery/Energy Technology Joint General Session Held During the 216th Meeting of the Electrochemical Society (ECS), Vienna, Austria, 4–9 October 2009; pp. 121–127.
40. Ma, S.B.; Lee, D.J.; Roev, V.; Im, D.; Doo, S.G. Effect of porosity on electrochemical properties of carbon materials as cathode for lithium-oxygen battery. *J. Power Sources* **2013**, *244*, 494–498. [[CrossRef](#)]
41. Jung, C.Y.; Zhao, T.S.; An, L.; Zeng, L.; Wei, Z.H. Screen printed cathode for non-aqueous lithium-oxygen batteries. *J. Power Sources* **2015**, *297*, 174–180. [[CrossRef](#)]
42. Chen, J.F.; Zhang, Y.R.; Tan, L.; Zhang, Y. A Simple Method for Preparing the Highly Dispersed Supported Co<sub>3</sub>O<sub>4</sub> on Silica Support. *Ind. Eng. Chem. Res.* **2011**, *50*, 4212–4215. [[CrossRef](#)]
43. Wang, L.X.; Ara, M.; Wadumesthrige, K.; Salley, S.; Ng, K.Y.S. Graphene nanosheet supported bifunctional catalyst for high cycle life Li-air batteries. *J. Power Sources* **2013**, *234*, 8–15. [[CrossRef](#)]
44. Awan, Z.; Ghouri, Z.K.; Hashmi, S. Influence of Ag nanoparticles on state of the art MnO<sub>2</sub> nanorods performance as an electrocatalyst for lithium air batteries. *Int. J. Hydrogen Energy* **2018**, *43*, 2930–2942. [[CrossRef](#)]

45. Xu, Z.J.; Yang, L.; Jin, Q.R.; Hu, Z.H. Improved capacitance of NiCo<sub>2</sub>O<sub>4</sub>/carbon composite resulted from carbon matrix with multilayered graphene. *Electrochim. Acta* **2019**, *295*, 376–383. [[CrossRef](#)]
46. Devaguptapu, S.V.; Hwang, S.; Karakalos, S.; Zhao, S.; Gupta, S.; Su, D.; Xu, H.; Wu, G. Morphology Control of Carbon-Free Spinel NiCo<sub>2</sub>O<sub>4</sub> Catalysts for Enhanced Bifunctional Oxygen Reduction and Evolution in Alkaline Media. *ACS Appl. Mater. Interfaces* **2017**, *9*, 44567–44578. [[CrossRef](#)] [[PubMed](#)]
47. Zhang, W.G.; Xu, J.L.; Wang, H.Z.; Yao, S.W. CNT anchored by NiCo<sub>2</sub>O<sub>4</sub> nanoparticles with hybrid structure for ultrahigh-performance supercapacitor. *J. Mater. Sci.-Mater. Electron.* **2020**, *31*, 5948–5957. [[CrossRef](#)]
48. Lee, H.; Lee, D.J.; Kim, M.; Kim, H.; Cho, Y.S.; Kwon, H.J.; Lee, H.C.; Park, C.R.; Im, D. High-Energy Density LiO<sub>2</sub> Battery with a Polymer Electrolyte-Coated CNT Electrode via the Layer-by-Layer Method. *ACS Appl. Mater. Interfaces* **2020**, *12*, 17385–17395. [[CrossRef](#)]
49. Lee, J.H.; Jung, H.W.; Kim, I.S.; Park, M.; Kim, H.S. Electrochemical Evaluation of Surface Modified Free-Standing CNT Electrode for LiO<sub>2</sub> Battery Cathode. *Energies* **2021**, *14*, 4196. [[CrossRef](#)]
50. Xiao, X.; Li, X.H.; Wang, J.X.; Yan, G.C.; Wang, Z.X.; Guo, H.J.; Liu, Y. Robust assembly of urchin-like NiCo<sub>2</sub>O<sub>4</sub>/CNTs architecture as bifunctional electrocatalyst in Zn-Air batteries. *Ceram. Int.* **2020**, *46*, 6262–6269. [[CrossRef](#)]

**Disclaimer/Publisher’s Note:** The statements, opinions and data contained in all publications are solely those of the individual author(s) and contributor(s) and not of MDPI and/or the editor(s). MDPI and/or the editor(s) disclaim responsibility for any injury to people or property resulting from any ideas, methods, instructions or products referred to in the content.